Observation of Noise Correlated by the Hawking Effect in a Water Tank

L.-P. Euvé,[1,*] F. Michel,[2,†] R. Parentani,[2,‡] T. G. Philbin,[3,§] and G. Rousseaux[1,‖]
[1]Institut Pprime, UPR 3346, CNRS-Université de Poitiers-ISAE ENSMA 11 Boulevard Marie et Pierre Curie-Téléport 2, BP 30179, 86962 Futuroscope Cedex, France
[2]Laboratoire de Physique Théorique, CNRS, Univ. Paris-Sud, Université Paris-Saclay, 91405 Orsay, France
[3]Physics and Astronomy Department, University of Exeter, Stocker Road, Exeter EX4 4QL, United Kingdom
(Received 30 November 2015; revised manuscript received 29 July 2016; published 13 September 2016)

We measured the power spectrum and two-point correlation function for the randomly fluctuating free surface on the downstream side of a stationary flow with a maximum Froude number $F_{\max} \approx 0.85$ reached above a localized obstacle. On such a flow the scattering of incident long wavelength modes is analogous to that responsible for black hole radiation (the Hawking effect). Our measurements of the noise show a clear correlation between pairs of modes of opposite energies. We also measure the scattering coefficients by applying the same analysis of correlations to waves produced by a wave maker.

DOI: 10.1103/PhysRevLett.117.121301

The Hawking effect in laboratory analogues of event horizons [1] has been well studied theoretically [2,3] and experiments have been performed in different systems [4–6]. Analogue horizons are created when waves propagate in a stationary counterflowing medium: at points where the flow speed reaches that of the wave, the latter is blocked and converted to other branches of the dispersion relation. At low frequency, this gives rise to a mode amplification (an over-reflection [7]) which involves a negative-energy wave [4,8–10], and which is at the root of the Hawking effect [11]. Importantly, the scattered waves of opposite energy are correlated with each other [12]. As a result, when dealing with a noisy system, the two-point correlation function of the fluctuating quantity displays specific patterns both in space-time and in Fourier space [13–18]. We here consider surface waves on a stationary countercurrent of water in a linear tank. Our work is inspired by the theoretical Refs. [9,19–21] and builds on the experiments reported in Refs. [4,6,22,23]. As in these experiments, the flow velocity near the blocking point decreases along the direction of the flow. This means that we work with an analogue white hole (the time reversed of a black hole).

Ignoring the surface tension, and assuming that the flow is incompressible and irrotational, the dispersion relation which relates the angular frequency ω and the wave vector k is

$$(\omega - Uk)^2 = gk \tanh(kh), \tag{1}$$

where U is the flow velocity, h the water depth, and g the gravitational acceleration, see the Supplemental Material [24] for some explanation about this relation, and its associated wave equation. In a flow to the right, i.e., $U > 0$, for a fixed ω, see the dotted horizontal line in Fig. 1, the three roots k_I, k_B, and k_H describe counterpropagating waves, i.e., waves with a group velocity oriented to the left in *the co-moving frame at rest with the fluid* [3,4,9]. Instead k_R describes a copropagating mode which shall play no role in the sequel. There are also transverse modes, which have an effective mass [28] proportional to their transverse wave vector $k_\perp$.

In stationary inhomogeneous flows, such as that of Fig. 2, ω is conserved. For fixed $\omega > 0$, the roots k_I and k_B merge at a point in the tank where U becomes sufficiently large [21]. This merging describes an incident long-wavelength mode I coming from the right, that is blueshifted into a B mode with opposite group velocity $d\omega/dk$ *in the laboratory frame* (the slope of the curves in Fig. 1): the well-known wave blocking [9,29]. We emphasize here that the wave number k_B of the scattered mode is much larger than k_I characterizing the incident wave. This large blueshifting is the typical signature of analogue white hole flows [10,30]. Importantly, for sufficiently low ω, the wave blocking is accompanied by a nonadiabatic effect producing an additional mode which also has a large wave vector: k_H. This mode has a negative frequency $\omega - Uk$ as measured in the fluid frame, see Fig. 1, and thus carries a negative-energy [4,8–10]. Because the total wave energy is conserved, this conversion implies an amplification of the B mode. This is in strict analogy with the Hawking effect. However, it is difficult experimentally to have a flow that will block waves at all frequencies and in experiments to date [4,6,23] only waves above a critical frequency $\omega_{\min}$ were (essentially) blocked, see the Supplemental Material [24]. Above $\omega_{\min}$, as we shall see, the main effect is the conversion of incident I modes into B and H. This effect was reported in Ref. [6] both below and above $\omega_{\min}$.

This conversion can be stimulated by an incident wave I generated by a wave maker, as was done in Refs. [4,6]. In contrast, the quantum Hawking effect, of fundamental interest for black holes [11], arises from the amplification

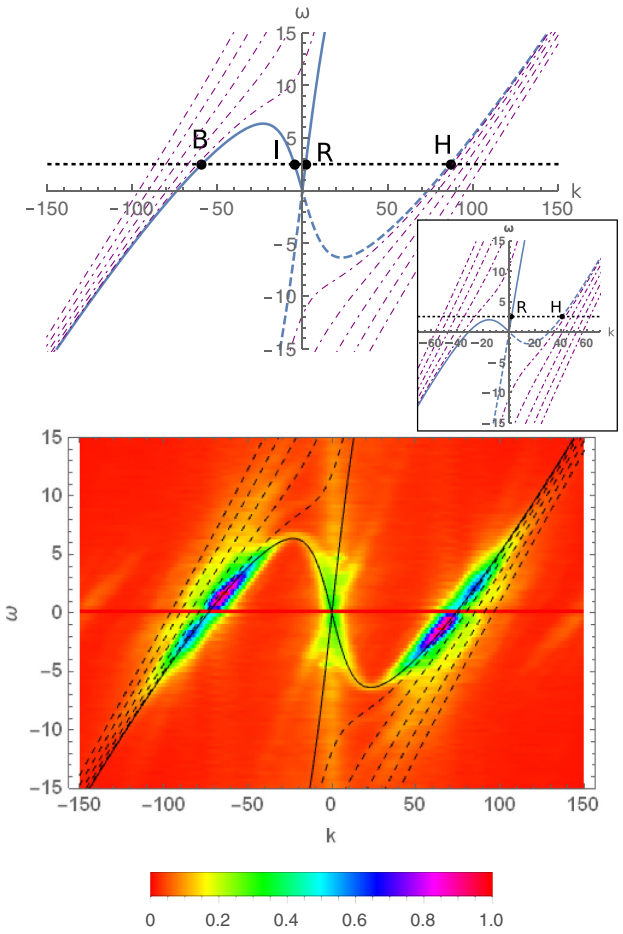

FIG. 1. Top: Dispersion relation in the homogeneous flow on the downstream side of the obstacle. k is in m^{-1} and the angular frequency ω in Hz. The effective parameters [see text below Eq. (2) for definition] are $U_{\mathrm{eff}} = 0.37\ \mathrm{m \cdot s^{-1}}$ and $h_{\mathrm{eff}} = 88$ mm. The blue continuous (dashed) lines correspond to Eq. (1) with positive (negative) $\omega - Uk$. The four dots labeled by B, I, R, H give the roots k_a for a fixed $\omega > 0$ indicated by a dotted horizontal line. Purple, dot-dashed lines describe transverse modes with an even number of nodes in the transverse direction (those with an odd number are not detected by our experimental setup). The inset shows the same dispersion relation for $h = 59$ mm, i.e., beyond the turning point for the frequency materialized by the dashed line. Bottom: Square root of the noise power $\mathcal{P}(\omega, k)$ divided by its maximum value and measured on the downstream side of the obstacle, see Fig. 2 and Eq. (2).

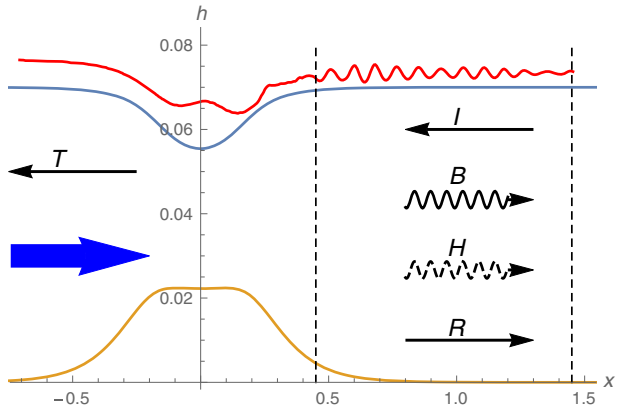

FIG. 2. Plots of the obstacle (orange line) and the observed free surface (red line, see also the Figure S3 in the Supplemental Material [24]) in meters. The two dashed vertical lines indicate the region used to study the fluctuations of the free surface δh. The blue, thick arrow shows the direction of the flow. Thin arrows show the orientation of the group velocity (measured in the laboratory frame) of the various modes produced by the scattering of the incident I mode. The letters I, B, H, R have the same meaning as in Fig. 1. The T arrow represents the transmitted wave in the upstream side. The blue curve gives the free surface chosen for determining the obstacle, see text for explanation.

of vacuum fluctuations and gives rise to pairs of entangled quanta with opposite energy [12]. Surface waves in the water tank are not suitable to observe the quantum Hawking effect. But just as the quantum vacuum provides the horizon with an irreducible input, there is a stationary background noise of surface waves in the inhomogeneous flow created by both the turbulent flow and the underwater obstacle, see Fig. 1 lower panel. Because of the mode conversion near the blocking point, this noise should be *correlated*. When measured in the downstream homogeneous region, see Fig. 2, these correlations are nonvanishing when the k_a's are evaluated at the same value of ω [14,15,17], see Fig. 3 and the Supplemental Material [24].

Our experiments were performed in the water channel of the Pprime Institute (for more details, see Supplemental Material [24]). The obstacle used to obtain an inhomogeneous flow was designed following the procedure outlined in appendix A of Ref. [21]. It relies on the hodograph transformation for a 2D inviscid, irrotational, incompressible flow [31]. The shape of the obstacle is determined by the profile of the free surface, the asymptotic water depth, and flow velocity, see Fig. 2. The main advantage of this obstacle over the one used in Refs. [6,23] is that it supports a flow with a relatively large Froude number: 0.86 ± 0.03 in the present experiment instead of 0.67 ± 0.02 see Sect. III D in Ref. [23]. In addition, it produces a smaller static surface deformation, or undulation [10,32], with a peak-to-peak amplitude of a few millimeters (see Supplemental Material [24]). The descending slope of the obstacle also has a larger maximum gradient: the slope of $c - U$, giving the analogue surface gravity in transcritical flows [21], has a maximum of 2 Hz instead of 1.2 Hz as used in Ref. [6] (here $c = \sqrt{gh}$ is the velocity of long-wavelength waves in the fluid frame).

We measured the fluctuations of the water height $\delta h(x, t)$, defined as the deviation from the time-averaged value of $h(x, t)$, in the downstream constant-flow region shown in Fig. 2. We first studied the noise power (which is proportional to the wave action [33]) defined by

$$\mathcal{P}(\omega, k) \equiv \langle |\delta\tilde{h}(\omega, k)|^2 \rangle \times S_k^{-2}. \qquad (2)$$

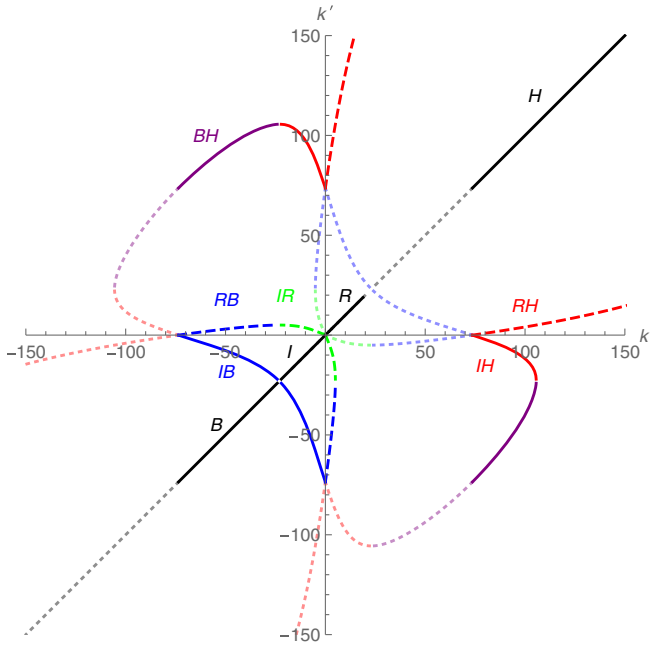

FIG. 3. Here we show the loci where k, k' are two roots of Eq. (1) for $\omega \in \mathbb{R}^+$ in a flow with the same parameters as in Fig. 1. The oblique black segments show $k = k'$ for the four modes B, I, R, H. The three continuous curves show $\{k, k'\} = \{k_I, k_B\}$ (blue), $\{k_I, k_H\}$ (red), $\{k_B, k_H\}$ (purple), while the dashed lines $\{k_I, k_R\}$ (green), $\{k_R, k_B\}$ (blue), and $\{k_R, k_H\}$ (red), involve the mode k_R. Dotted lighter curves correspond to $\omega < 0$. They are obtained from correlations with positive ω by $(k, k') \to (-k, -k')$.

Here, $\delta\tilde{h}(\omega, k)$ is the Fourier transform of $\delta h(t, x)$ and $S_k = |gk \tanh(kh)|^{1/4}$ is the structure factor relating plane waves to unit-norm modes when working at fixed k [10,21]. The Fourier transform in time is computed using a rectangular window, while we used a Hamming window function [34] with support $x \in [0.45\text{ m}, 1.45\text{ m}]$ to compute the spatial transform (see Supplemental Material [24]). The mean value is computed by dividing the data into 80 pieces of equal duration (12.5 s) and averaging over them. In former studies of the noise [22,35], this averaging was not performed. As a result the plots showed random values of $|\delta\tilde{h}(\omega, k)|^2$ as opposed to its mean. The square root of $\mathcal{P}(\omega, k)$ is shown in the lower panel of Fig. 1. The typical amplitude of $|\delta h(x, t)|$ in the observation window is a few tenths of millimeters.

Although the upstream water height and flow velocity were $h_{\text{up}} = 74$ mm and $U_{\text{up}} = 0.31\ \text{m} \cdot \text{s}^{-1}$, the dispersion relation of Fig. 1 has been drawn with the effective values $h_{\text{eff}} = 88$ mm and $U_{\text{eff}} = 0.37\ \text{m} \cdot \text{s}^{-1}$, chosen to match the observed wave numbers. The agreement of the dispersion relation with the three counterpropagating modes I, B, and H is clear for all values of ω. We expect that the differences with h_{up} and U_{up} are due to boundary layer, vorticity, and turbulent effects. When using h_{eff} and U_{eff}, we find that the value of ω for which the two roots k_I and k_B merge on top of the obstacle (respectively in the downstream asymptotic region) is $\omega_{\min} \approx 0.8$ Hz (respectively $\omega_{\max} \approx 5$ Hz).

We then measured the two-point correlation function evaluated at the same frequency and two different wave vectors:

$$G_2(\omega; k, k') \equiv |\langle \delta\tilde{h}(\omega, k) \delta\tilde{h}(\omega, k')^* \rangle| \times (S_k S_{k'})^{-1}. \quad (3)$$

In the left plot of Fig. 4, we show $G_2(\omega; k, k')$ in the (k, k') plane for $\omega = 2.5$ Hz. Using the effective values h_{eff} and U_{eff}, the nonvanishing correlations in the k, k' plane are found along the lines drawn in Fig. 3, as expected. We note that the B and H modes of opposite energy are well correlated. We also note that the long-wavelength modes I and R are correlated with both B and H modes. However, we cannot clearly separate the contributions of I and R modes. Since numerical simulations (see Supplemental Material [24]) indicate that the copropagating (R) mode is only weakly coupled to I, B, and H, in what follows, we only study the power and the strength of correlations of these three modes.

In the upper plot of Fig. 5 we show $n_a(\omega) \equiv \mathcal{P}(\omega, k_a)/|dk_a/d\omega|$ as a function of ω, where $k_a(\omega)$ are the three counterpropagating roots. This quantity gives, up to an overall factor, the mean number of quasiparticles per unit angular frequency interval [10,21]. The power spectra of the two dispersive modes B and H are comparable except in a domain near $\omega_{\min} \approx 0.8$ Hz where there are more B modes. The hydrodynamical I modes have less power by a factor $\sim$10, except below $\omega_{\min}$ where their power is much larger. (In the absence of an obstacle, the observed noise power is completely dominated by the hydrodynamical modes I and R, and there are no significant correlations between I and B, H modes, see Supplemental Material [24]).

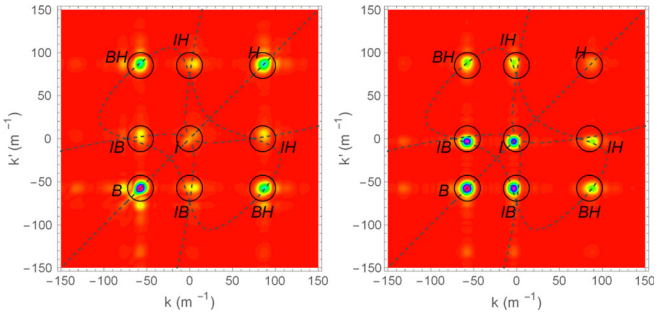

FIG. 4. In the left panel, we show the noise correlation function of Eq. (3) for $\omega = 2.5$ Hz. The color scale is the same as in Fig. 1. Dashed lines show the dispersion relation in the (k, k') plane, see Fig. 3. The circles are centered on (k_ω, k'_ω) where k_ω and k'_ω are two roots of the dispersion relation for the considered frequency ω. The letters B and H designate the power of the short-wavelength modes with opposite energies, and BH their correlations. In the right panel, we show again Eq. (3) when the wave maker is sending the incident wave I with $\omega = 2.5$ Hz. The IB and IH correlations are clearly visible.

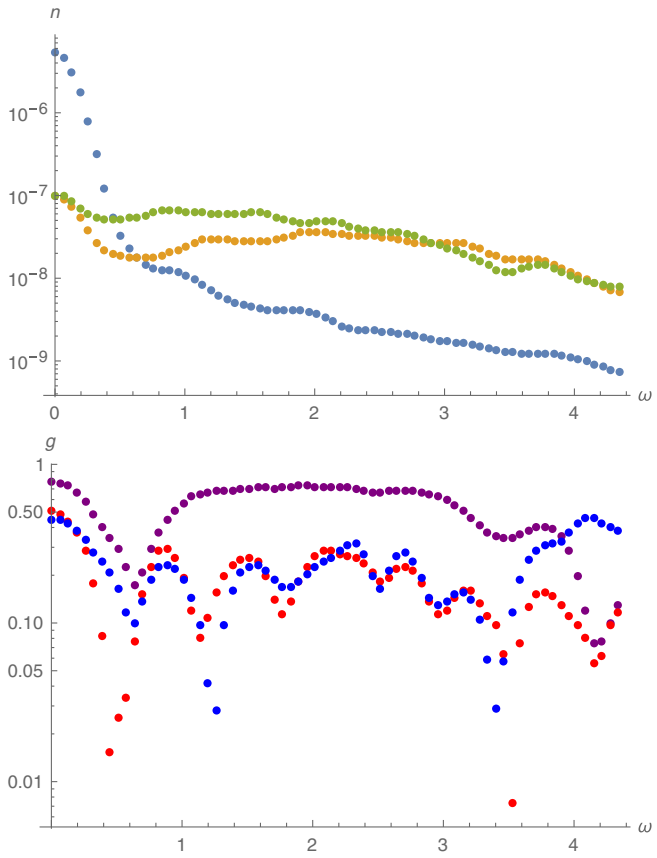

FIG. 5. The noise power $n_a(\omega)$ (upper plot, in $m^3 \cdot s^2$) and the relative strength of the correlations of Eq. (4) (lower plot), in logarithmic scale, for the counterpropagating modes I, B, and H. In the upper plot, the power of I is in blue, that of B in green, and in bronze that of H. In the lower plot, the correlations BH are in purple, IB in blue, and IH in red. We estimate that the uncertainties on g_2 are of order 0.1.

To quantify the strength of the correlations, we study the ratio of the cross-correlations over the square root of the product of the autocorrelations

$$g_2(\omega; a, b) \equiv \frac{G_2(\omega; k_a, k_b)}{\sqrt{G_2(\omega; k_a, k_a) G_2(\omega; k_b, k_b)}}, \qquad (4)$$

where $k_a(\omega)$, $k_b(\omega)$ are two roots for a given ω. For any statistical ensemble, g_2 is necessarily smaller than 1. As explained in the Supplemental Material [24], g_2 involves the classical counterparts of the observables which are currently used in quantum settings to assert that the state of the scattered waves $k_a(\omega)$, $k_b(\omega)$ is entangled [15–18]. The lower plot of Fig. 5 shows three types of correlations: the BH correlations are stronger than the two other ones, since $g_2(\omega; B, H)$ is close to 0.7 (except near 0.6 Hz). This indicates that 70% of B and H modes are in correlated BH pairs. The IH and IB correlations are below 0.3 over most of the frequency domain. This implies that more than 50% of BH pairs do not come from observed I modes with $k_\perp = 0$. It probably means that a significant fraction of BH pairs have a nonvanishing $k_\perp$. (At present we are not able to separate the contributions of B and H modes with and without transverse wave number, as the corresponding curves on the dispersion relation are very close to each other, see Fig. 1.) Some BH pairs should also be produced by *incident* waves H and R from the left. In addition, not all the incident I-mode noise is taken into account if some of it is generated by fluctuations in the region $x < 0.45$ m. An effective description of this generation could be obtained from adapting to the present case the driven-damped wave equation of Ref. [36].

The properties of the scattering can be more clearly studied when sending an I wave towards the obstacle, as was done in Refs. [4,6,23]. The corresponding values of G_2 are shown in the right panel of Fig. 4 for $\omega \approx 2.5$ Hz $> \omega_{\min}$. The power of the reflected B wave is close to that of the incident one, as expected from the validity of the adiabatic approximation in this regime [3]. The negative-energy H wave remains relatively small in amplitude. However, HI and HB correlations are clearly visible, showing that H and B waves are produced by the analogue Hawking effect. This is further clarified by the analysis of the scattering coefficients presented in the Supplemental Material [24].

To summarize, we observed the statistical properties of the water depth fluctuations downstream from an obstacle in a flow with a large maximum Froude number. The negative-energy modes H are highly populated, strongly correlated with the positive-energy modes B, but more weakly correlated with the I modes. The noise correlations have the main features expected from the Hawking effect, whose correlations we observed also in the stimulated case with a wave maker. Further experiments and theoretical work are required to clarify all of the processes behind these observations.

We thank Y. Stepanyants for comments. We acknowledge support from the University of Poitiers (ACI UP on Wave-Current Interactions 2013-2014), the Interdisciplinary Mission of CNRS (PEPS PTI 2014 DEMRATNOS), the University of Tours (ARC Poitiers-Tours 2014-2015), the French national research agency (ANR) HARALAB (N° ANR-15-CE30-0017-04), the FEDER 35790-2012, and a FQXi grant of the Silicon Valley Community Foundation.

*leo.paul.euve@univ-poitiers.fr
†florent.michel@th.u-psud.fr
‡Renaud.Parentani@th.u-psud.fr
§T.G.Philbin@exeter.ac.uk
‖germain.rousseaux@univ-poitiers.fr

[1] W. G. Unruh, Phys. Rev. Lett. **46**, 1351 (1981).
[2] C. Barcelo, S. Liberati, and M. Visser, Living Rev. Relativ. **8**, 12 (2005); S. J. Robertson, J. Phys. B **45**, 163001 (2012).

[3] A. Coutant, R. Parentani, and S. Finazzi, Phys. Rev. D **85**, 024021 (2012).

[4] G. Rousseaux, C. Mathis, P. Maïssa, T. G. Philbin, and U. Leonhardt, New J. Phys. **10**, 053015 (2008).

[5] T. G. Philbin, C. Kuklewicz, S. Robertson, S. Hill, F. König, and U. Leonhardt, Science **319**, 1367 (2008); F. Belgiorno, S. L. Cacciatori, G. Ortenzi, V. G. Sala, and D. Faccio, Phys. Rev. Lett. **104**, 140403 (2010); O. Lahav, A. Itah, A. Blumkin, C. Gordon, S. Rinott, A. Zayats, and J. Steinhauer, Phys. Rev. Lett. **105**, 240401 (2010); J. Steinhauer, Nat. Phys. **10**, 864 (2014); H. S. Nguyen, D. Gerace, I. Carusotto, D. Sanvitto, E. Galopin, A. Lemaître, I. Sagnes, J. Bloch, and A. Amo, Phys. Rev. Lett. **114**, 036402 (2015).

[6] S. Weinfurtner, E. W. Tedford, M. C. J. Penrice, W. G. Unruh, and G. A. Lawrence, Phys. Rev. Lett. **106**, 021302 (2011).

[7] R. D. Acheson, J. Fluid Mech. **77**, 433 (1976).

[8] A. L. Fabrikant and Y. A. Stepanyants, *Propagation of Waves in Shear Flows* (World Scientific, Singapore, 1998).

[9] J.-C. Nardin, G. Rousseaux, and P. Coullet, Phys. Rev. Lett. **102**, 124504 (2009).

[10] A. Coutant and R. Parentani, Phys. Fluids **26**, 044106 (2014).

[11] S. W. Hawking, Nature (London) **248**, 30 (1974).

[12] R. Brout, S. Massar, R. Parentani, and Ph. Spindel, Phys. Rep. **260**, 329 (1995); Phys. Rev. D **52**, 4559 (1995).

[13] I. Carusotto, S. Fagnocchi, A. Recati, R. Balbinot, and A. Fabbri, New J. Phys. **10**, 103001 (2008).

[14] J. Macher and R. Parentani, Phys. Rev. A **80** (2009) 043601.

[15] J. R. M. deNova, I. Zapata, and F. Sols, Phys. Rev. A **89**, 043808 (2014).

[16] X. Busch and R. Parentani, Phys. Rev. D **89**, 105024 (2014).

[17] D. Boiron, A. Fabbri, P.-É. Larré, N. Pavloff, C. I. Westbrook, and P. Zin, Phys. Rev. Lett. **115**, 025301 (2015).

[18] J. Steinhauer, Nat. Phys., doi:10.1038/nphys3863 (2016).

[19] R. Schützhold and W. G. Unruh, Phys. Rev. D **66**, 044019 (2002).

[20] G. Rousseaux, P. Maïssa, C. Mathis, P. Coullet, T. G. Philbin, and U. Leonhardt, New J. Phys. **12**, 095018 (2010).

[21] F. Michel and R. Parentani, Phys. Rev. D **90**, 044033 (2014).

[22] P.-J. Faltot, R. Bellanger, J.-M. Mougenot, and G. Rousseaux, Proceedings des 13èmes Journées Génie Côtier Génie Civil à Dunkerque en Juillet 2014. Session d'Hydrodynamique Côtière, edited by D. Levacher, M. Sanchez, A. Hequette et Yves Lalaut (2014), 79–92, http://www.paralia.fr/jngcgc/13_10_faltot.pdf.

[23] L.-P. Euvé, F. Michel, R. Parentani, and G. Rousseaux, Phys. Rev. D **91**, 024020 (2015).

[24] See Supplemental Material, which includes Refs. [25–29], at http://link.aps.org/supplemental/10.1103/PhysRevLett.117.121301 for the main properties of the wave equation, details on the experimental setup, a discussion of the scattering coefficients and nonlinear effects, and a comparison with [18].

[25] G. Heinzel, A. Rüdiger, and R. Schilling, Spectrum and spectral density estimation by the Discrete Fourier transform (DFT), including a comprehensive list of window functions and some new at-top windows (2002), http://edoc.mpg.de/395068.

[26] T. H. C. Herbers S. Elgar and R. T. Guza, J. Phys. Oceanogr. **32**, 1181 (2002).

[27] F. Michel, J.-F. Coupechoux, and R. Parentani, arXiv:1605.09752.

[28] G. Jannes, P. Maïssa, T. G. Philbin, and G. Rousseaux, Phys. Rev. D **83**, 104028 (2011).

[29] M. W. Dingemans, *Water Wave Propagation Over Uneven Bottoms* (World Scientific, Singapore, 1997).

[30] C. Mayoral, A. Recati, A. Fabbri, R. Parentani, R. Balbinot, and I. Carusotto, New J. Phys. **13**, 025007 (2011).

[31] W. G. Unruh, Lect. Notes Phys. **870**, 63 (2013).

[32] W. G. Unruh, Phil. Trans. R. Soc. A **366**, 2905 (2008).

[33] F. P. Bretherton and C. J. R. Garrett, Proc. R. Soc. A **302**, 529 (1968).

[34] K. M. M. Prabhu, *Window Functions and their Applications in Signal Processing* (CRC Press, Boca Raton, Florida, 2013).

[35] S. Weinfurtner, E. W. Tedford, M. C. J. Penrice, W. G. Unruh, and G. A. Lawrence, Lect. Notes Phys. **870**, 167 (2013).

[36] S. Robertson and R. Parentani, Phys. Rev. D **92**, 044043 (2015).